Equilibration of weakly nonlinear salt fingers

TIMOUR RADKO†

Department of Oceanography, Naval Postgraduate School, Monterey, CA 93943, USA

An analytical model is developed to explain the equilibration mechanism of the salt finger instability in unbounded temperature and salinity gradients. The theory is based on the weakly nonlinear asymptotic expansion about the point of marginal instability. The proposed solutions attribute equilibration of salt fingers to a combination of two processes: (i) the triad interaction and (ii) spontaneous development of the mean vertical shear. The non-resonant triad interactions control the equilibration of linear growth for moderate and large values of Prandtl number (Pr) and for slightly unstable parameters. For small Pr and/or rigorous instabilities, the mean shear effects become essential. It is shown that, individually, neither the mean field nor the triad interaction models can accurately describe the equilibrium patterns of salt fingers in all regions of the parameter space. Therefore, we propose a new hybrid model, which represents both stabilizing effects in a single framework. The resulting solutions agree with the fully nonlinear numerical simulations over a wide range of governing parameters.

1. Introduction

Double diffusion is the instability of a stratified fluid at rest whose density is determined by two components diffusing at different rates. Stern (1960) demonstrated that such a configuration can be unstable even if the density of the fluid is increasing downwards. The resulting double-diffusive convection has long been recognized as a significant, and in many cases dominant, mixing process in the ocean. In the subtropical oceans, hot salty water is often located above cold and fresh. Thus, the faster diffuser (temperature T) is stabilizing and the slower diffuser (salinity S) is destabilizing, resulting in the salt finger form of double-diffusive convection, which is the main focus of our discussion. In addition to oceanographic applications, the compositionally driven double-diffusive convection affects the heat and material transport in a variety of other geo- and astrophysical fluid systems, from magmatic melts (Tait & Jaupart 1989) to the interiors of giant planets and stars (Guillot 1999; Vauclair 2004; Charbonnel & Zahn, 2007; Stancliffe *et al.* 2007).

A fundamental problem of the double-diffusive convection theory, in all its forms and applications, concerns the equilibration of primary instability and the onset of statistically steady convection. According to linear instability theory (Stern 1960; Schmitt 1979), the fastest growing salt fingers appear in the form of narrow vertical streams – the elevator modes. These vertical modes, in turn, also become unstable (Holyer 1984). Laboratory (e.g. Krishnamurti 2003) and modelling studies (Stern &

† Email address for correspondence: tradko@nps.edu

Simeonov 2005) suggest that the secondary instabilities of the elevator mode ultimately arrest its growth and thereby control the characteristics of the equilibrium state. However, the mechanism of interaction between primary and secondary instabilities is still unclear, and the explicit prediction of the equilibrium amplitude of salt fingers as a function of the background parameters is lacking.

This study systematically explores a broad region of the parameter space, which includes both the oceanographically relevant moderate values of the Prandtl number (Pr) as well as low Pr realized in the interior of stars and giant planets (Schmitt 1983; Merryfield 1995). While the difference in parameters relevant for geophysical and astrophysical applications is substantial – ultimately resulting in different equilibrium dynamics – it is of interest to discuss both systems in terms of a unified theory. We attempt to explain the equilibrium patterns and magnitudes of salt fingers by developing a weakly nonlinear asymptotic expansion pivoted about the point of marginal instability. The proposed solutions attribute the equilibration to a combination of two stabilizing effects: (i) the triad or mode–mode interaction and (ii) the adverse action of vertical shear, spontaneously developing as a result of secondary salt finger instabilities. The relative importance of the triad and mean field effects varies with governing parameters. Triad interactions control the equilibration of the linear growth for moderate and large values of Prandtl number and for the marginal instability, whereas the mean field effects become essential for small Pr and/or in the strongly nonlinear regime.

This study indicates that the asymptotic nonlinear models based entirely on the triad or entirely on the mean field equilibration mechanisms have only limited success in reproducing the numerical results. However, a more general expansion, which takes into account both effects, agrees well with the corresponding fully nonlinear simulations over a wide range of governing parameters. We predict that the vertical heat-salt fluxes rapidly decrease with the density ratio $R_\rho = \alpha \bar{T}_z / \beta \bar{S}_z$ and have a complicated non-monotonic dependence on the Prandtl number $Pr = \nu / k_T$. In this paper, $(\bar{T}_z, \bar{S}_z)$ denote the background gradients of temperature and salinity, (α, β) are the expansion/contraction coefficients, (k_T, k_S) are the molecular diffusivities of heat and salt and ν is the viscosity.

Before presenting details of the proposed theory, it should be emphasized that our model describes only the local effects that are controlled by the local *T*-*S* gradients; we are concerned here with spatial scales comparable to the characteristic salt finger width. As argued in Stern, Radko & Simeonov (2001), solutions for individual fingers are essential in formulating the 'small domain' flux-gradient laws and inclusion of much greater scales in the model may reveal their secondary instabilities. The large-scale instabilities, in turn, can modify the uniform background stratification (Merryfield 2000; Radko 2003, 2005), spontaneously generating stepped structures known as thermohaline staircases. These effects, however, are beyond the scope of our paper.

The proposed theory should also be clearly distinguished from the earlier studies (Veronis 1965; Proctor & Holyer 1986; Radko & Stern 2000; Balmforth *et al.* 2006) of a model in which the finger layer is vertically bounded by rigid surfaces – a set-up similar to the classical Rayleigh convection problem. These rigid boundary conditions filter out the fastest growing elevator mode, leading to fundamental differences between bounded and unbounded dynamics. While the bounded configuration could be relevant for some lab experiments (see the discussion in Radko & Stern 2000), the unbounded model is more representative of typical oceanic and astrophysical systems where the scale of fingering zones greatly exceeds the scale of individual fingers.

Dynamical peculiarities caused by the unbounded character of the system render some standard methods of the nonlinear stability analysis inapplicable for our problem, motivating the development of new techniques. For instance, in the thermal convection theory (Malkus & Veronis 1958), the asymptotic expansion opens with the fastest growing normal mode. The nonlinear interaction modifies the mean (horizontally averaged) temperature distribution and ultimately leads to the equilibration of linear growth. Analogous models have been developed for a great variety of the stability problems (reviewed by Drazin & Reid 1981, among others). Unfortunately, this direct approach cannot be applied to the unbounded salt finger model, where the fastest growing elevator mode represents an *exact* solution of the nonlinear governing equations. As a result, even in the weakly nonlinear limit, our system does not reduce to a single-model amplitude equation of Landau type (Landau 1944). Instead, it retains the form of full partial differential equations. However, these asymptotic equations are considerably simpler and more transparent than the original set. The weakly nonlinear models analytically represent the dependence of all quantities on the background density ratio – one of the central problems in the double-diffusive convection theory.

The paper is set up as follows. In §2 we present preliminary two-dimensional numerical experiments focusing our inquiry on the equilibrium patterns of fully developed fingering convection and their dependence on the Prandtl number. In §3, we formulate two weakly nonlinear models that isolate specific mechanisms of equilibration – the triad interaction and the mean field mechanisms – and discuss their limitations. The equilibrium structure of the simulated salt fingers is explained by a hybrid model, which includes both stabilizing effects in a single framework (§4). Section 5 summarizes the results and conclusions.

2. Numerical simulations

Following Radko & Stern (1999), we separate the temperature and salinity fields into the basic state $(\bar{T}, \bar{S})$, representing a uniform vertical gradient, and a departure (T, S) from it. The two-dimensional Boussinesq equations of motion are expressed in terms of T, S and non-dimensionalized using $l = (k_T \nu / g \alpha \bar{T}_z)^{1/4}$, k_T/l and l^2/k_T as the scales of length, velocity and time respectively. The expansion/contraction coefficients are incorporated in (T, S), and $\alpha \bar{T}_z l$ is used as the scale for both temperature and salinity perturbations, resulting in

$$\begin{cases} \dfrac{\partial T}{\partial t} + J(\psi, T) + \dfrac{\partial \psi}{\partial x} = \nabla^2 T, \\[2mm] \dfrac{\partial S}{\partial t} + J(\psi, S) + \dfrac{1}{R_\rho} \dfrac{\partial \psi}{\partial x} = \tau \nabla^2 S, \\[2mm] \dfrac{\partial}{\partial t} \nabla^2 \psi + J(\psi, \nabla^2 \psi) = Pr \left[\dfrac{\partial}{\partial x}(T - S) + \nabla^4 \psi \right], \end{cases} \tag{1}$$

where ψ is the streamfunction and $J(a, b) = (\partial a / \partial x)(\partial b / \partial z) - (\partial a / \partial z)(\partial b / \partial x)$ is the Jacobian. This system is unstable with respect to the salt fingering (Stern 1960) for

$$1 < R_\rho < 1/\tau. \tag{2}$$

The key non-dimensional numbers governing the evolution of system (1) are the Prandtl number $Pr = \nu/k_T$, the diffusivity ratio $\tau = k_S/k_T$ and the background density ratio $R_\rho = \alpha \bar{T}_z / \beta \bar{S}_z$. We also assume that, in the absence of large-scale structures, fluxes are independent of the non-dimensional parameters related to the domain size (e.g. the Rayleigh number). The local flux-gradient laws are commonly used to
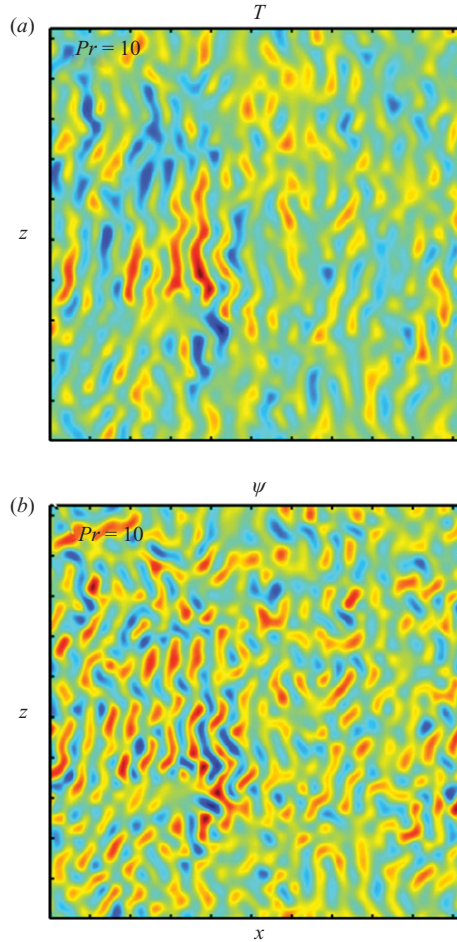
FIGURE 1. Instantaneous temperature T (a) and streamfunction ψ (b) for the numerical experiment with $Pr = 10$, $\tau = 1/3$. Red colour corresponds to high values; low values are shown in blue for both T and ψ.

parameterize the effects of salt fingering on the oceanic circulation and successful attempts have been made to validate the concept of an 'unbounded T-S gradient' in numerical simulations (Radko & Stern 1999).

To gain a preliminary understanding of the unbounded salt finger system and its dependence on (R_ρ, τ, Pr), the equations in (1) were solved numerically. We assume periodic boundary conditions for T, S and ψ in x and z and integrate the governing equations using a dealiazed pseudospectral method described in Stern & Radko (1998). In the following calculation, we use a diffusivity ratio of $\tau = 1/3$ which is higher than the heat/salt value ($\tau = 1/100$). This choice is dictated by considerations of convenience – otherwise it becomes necessary to resolve small scales set by the dissipation of salt in simulations and introduce two distinct dissipative scales in analytical models. As discussed in Stern et al. (2001) and Radko (2008), the use of a moderate diffusivity ratio is not expected to alter the fundamental physics and characteristics of salt fingering, as long as τ remains significantly less than unity.

Our first example (figure 1) is an experiment performed with the overall density ratio of $R_\rho = 2.8$ and the Prandtl number $Pr = 10$. The size of the square computational
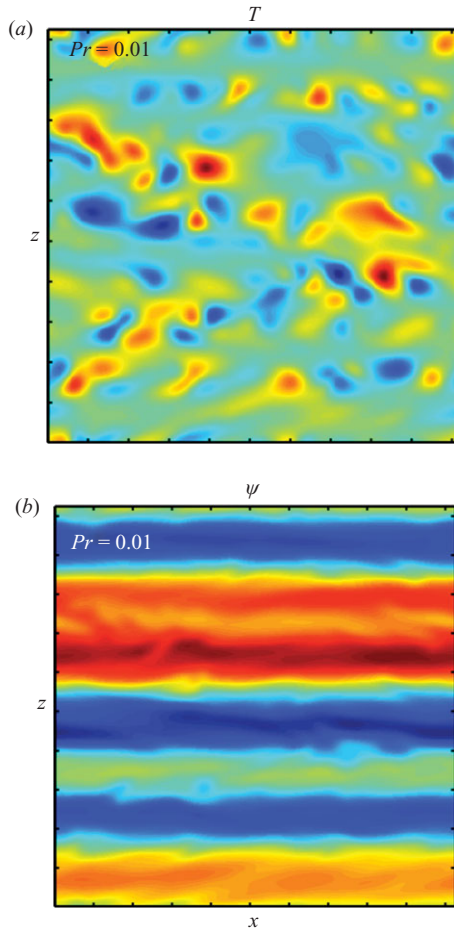
FIGURE 2. Same as in figure 1 but for $Pr = 0.01$. Note the appearance of the horizontally uniform bands in (b) representing the sheared horizontal flow.

domain ($L_x = L_z$) is equivalent to 16 linearly fastest growing finger wavelengths (d). The flow was resolved by a uniform mesh with $(N_x \times N_z) = (128 \times 128)$ elements, and the model was initialized from rest by a small-amplitude random computer-generated initial (T, S) distribution. After a few characteristic growth periods, active statistically steady double-diffusive convection was established. Figure 1(a) shows a typical instantaneous temperature field, which exhibits the characteristic signatures (e.g. Stern *et al.* 2001) of the fully developed fingering convection. Salt fingers are vertically elongated, irregular, and not visibly affected by the large-scale circulation patterns. Figure 1(b) presents the corresponding streamfunction, also dominated by the small-scale features whose scale is comparable to the salt finger width.

Figure 2 presents an analogous experiment performed with a much smaller Prandtl number $Pr = 0.01$; all other parameters are the same as in figure 1. The change in Prandtl number results in a dramatic alteration of the flow pattern. While the temperature field (figure 2a) is still dominated by small-scale features, salt fingers become more isotropic and irregular. The streamfunction field (figure 2b) reorganizes into the horizontally uniform bands representing sheared horizontal flow. The spontaneous development of the mean shear is a striking and persistent outcome of all experiments performed with low Pr. We note, in passing, that spontaneous

shear generation has also been observed in regular thermal convection experiments at large Rayleigh numbers (Krishnamurti & Howard 1981) and rationalized using of a low-order mathematical model (Howard & Krishnamurti 1986).

The difference in the equilibrium dynamics of salt fingers at high and low Prandtl numbers, illustrated in figures 1 and 2, requires an explanation. Guided by the classical treatments of the convection problems (e.g. Malkus & Veronis 1958), we explore the equilibration mechanisms by focusing on the marginally unstable regime.

3. Weakly nonlinear expansions: triad interaction and the mean field theory

To rationalize the key characteristics of the foregoing solutions (§2), we develop a weakly nonlinear theory based on an asymptotic expansion about the point of marginal instability for salt fingering $R_\rho \to \tau^{-1}$. We introduce a small parameter $\varepsilon = 1/R_\rho - \tau$ and search for a solution of the governing equations by expanding (T, S, ψ) in powers of ε. The governing equations are still given by (1), although the salinity equation is cast in a slightly modified form:

$$\frac{\partial S}{\partial t} + J(\psi, S) + (\tau + \varepsilon)\frac{\partial \psi}{\partial x} = \tau\nabla^2 S. \tag{3}$$

The space/time scales in this limit are determined on the basis of linear theory reviewed in Appendix A:

$$(x, z) = \varepsilon^{-1/4}(x_0, z_0), t = \varepsilon^{-3/2}t_0. \tag{4}$$

Next, we suppose that the leading order scale of the temperature is $T \sim \varepsilon^q$, where the exponent q is yet to be determined. The assumed balance of linear terms in the advection–diffusion equations (1) suggests scaling of the streamfunction as $\psi \sim \varepsilon^{1/4}T$ and the salinity as $S \sim T$. Thus,

$$\begin{cases} T = \varepsilon^q T_0 + \dots, \\ S = \varepsilon^q S_0 + \dots, \\ \psi = \varepsilon^{q+1/4}\psi_0 + \dots. \end{cases} \tag{5}$$

The value of q is ultimately controlled by the physics of equilibration. We now examine the two most common stabilizing processes – the triad and mean field interaction models.

3.1. *Triad interaction*

The triad models assume that the linear growth of each mode is countered by the nonlinear interaction of two other growing modes. Complex fluid dynamical systems, exemplified by fully developed fingering convection (see figures 1 and 2), necessarily involve a multitude of such interactions. The following asymptotic theory attempts to formalize the description of one-stage nonlinear interactions and their cumulative role in the selection of equilibrium patterns. This analytical development follows that in Radko and Stern (1999), who presented the weakly nonlinear three-dimensional model in the limit of infinite Prandtl number.

If it is the leading order nonlinearity that equilibrates the linear growth of unstable modes, then the terms $\partial T/\partial t$ and $J(\psi, T)$ in temperature equation (1) are of the same order, which, in view of (4) and (5), requires that

$$q = \frac{3}{4}. \tag{6}$$

The nonlinear interaction of the zero-order terms (5) also results in the generation of new (first-order) terms in the ε-expansion of (T, S, ψ). Their scale is deduced from the balance between the linear operator in the *T-S* equations acting on the first-order terms and the leading order nonlinearity:

$$\begin{cases} T = \varepsilon^{3/4} T_0 + \varepsilon^{7/4} T_1 + \dots, \\ S = \varepsilon^{3/4} S_0 + \varepsilon^{7/4} S_1 + \dots, \\ \psi = \varepsilon \psi_0 + \varepsilon^2 \psi_1 + \dots. \end{cases} \tag{7}$$

Next, the asymptotic series (7) are substituted in the governing equations (1) and the terms of the same order in ε are collected. The leading order $(\sim \varepsilon^{5/4})$ balance of the *T-S* equations yields the following diagnostic relationships between zero-order variables:

$$\begin{cases} T_0 = S_0, \\ \dfrac{\partial \psi_0}{\partial x_0} = \nabla_0^2 T_0, \end{cases} \tag{8}$$

where $\nabla_0^2 \equiv (\partial^2/\partial x_0^2) + (\partial^2/\partial z_0^2)$. At the next order $(\sim \varepsilon^{9/4})$, the *T-S* equations yield the following prognostic relationships:

$$\begin{cases} \dfrac{\partial T_0}{\partial t_0} + J_0(\psi_0, T_0) + \dfrac{\partial \psi_1}{\partial x_0} = \nabla_0^2 T_1, \\ \dfrac{\partial T_0}{\partial t_0} + J_0(\psi_0, T_0) + \dfrac{\partial \psi_0}{\partial x_0} + \tau \dfrac{\partial \psi_1}{\partial x_0} = \tau \nabla_0^2 S_1, \end{cases} \tag{9}$$

where $J_0(a, b) = (\partial a/\partial x_0)(\partial b/\partial z_0) - (\partial a/\partial z_0)(\partial b/\partial x_0)$. Note that we have also used $T_0 = S_0$ from (8). The leading order $(\sim \varepsilon^2)$ balance of the vorticity equation is given by

$$\frac{\partial}{\partial x_0}(T_1 - S_1) + \nabla_0^4 \psi_0 = 0. \tag{10}$$

Next, the salinity equation in (9) is divided by τ and subtracted from the temperature equation, and then $(T_1 - S_1)$ is eliminated using (10):

$$\left(\frac{1}{\tau} - 1\right) \frac{\partial}{\partial x_0} \left[\frac{\partial T_0}{\partial t_0} + J_0(\psi_0, T_0)\right] + \frac{1}{\tau} \frac{\partial^2 \psi_0}{\partial x_0^2} = \nabla_0^6 \psi_0. \tag{11}$$

Combining (11) with (8), we arrive at a closed system of equations for zero-order variables. This system contains no reference to ε or R_ρ, which means that the dependence of primary variables (T, S, ψ) on the density ratio is represented only by the rescaling factors in (5).

In order to determine whether (8) and (11) capture gross features of the original system (1), the asymptotic model was numerically integrated in time. To be consistent with earlier simulations (figures 1 and 2), the computational domain resolved 16 fastest growing finger wavelengths, the numerical grid consisted of (128×128) elements, the diffusivity ratio was $\tau = 1/3$, and the model was initialized from rest by a random computer-generated initial T_0 distribution. After a few characteristic growth periods, active statistically steady double-diffusive convection was established. The transition to the statistically steady regime is demonstrated by presenting (figure 3a) the time evolution of the rescaled temperature flux $F_{T0} = \langle w_0 T_0 \rangle$, where $\langle \dots \rangle$ denotes a spatial average. The flux equilibrated at
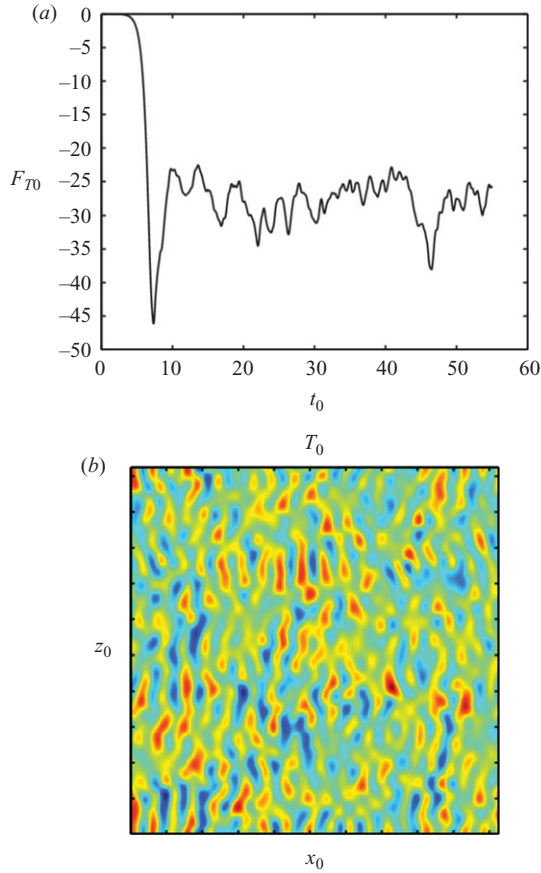
$$|F_{T0}| \approx 27.76. \tag{12}$$

FIGURE 3. Numerical integration of the triad model equations (§ 3.1). (*a*) Time record of the rescaled temperature flux, (*b*) instantaneous temperature field.

Figure 3(*b*) shows the typical instantaneous temperature field in the quasi-equilibrium regime ($t_0 = 50$), which exhibits the characteristically elongated salt fingers, reminiscent of the moderate Pr simulation of the original system (figure 1). However, the temperature field in figure 3(*b*) is qualitatively different from the low Pr simulation (figure 2), which suggests that the proposed nonlinear model based on the triad interaction may have a limited range of applicability.

To be more quantitative in analysing the asymptotic results, we performed a series of simulations with the original system (1) in which the density ratio was systematically varied. The Prandtl number was kept constant at $Pr = 1$ and all other parameters were the same as in figures 1–3. In each case, we recorded the equilibrium flux $F_T = \langle wT \rangle$, averaged in time, and the results (figure 4) were compared with the theoretical prediction:

$$F_T = \varepsilon^2 F_{T0}, \tag{13}$$

where the rescaled equilibrium flux F_{T0} is given in (12). The agreement between the original and asymptotic solutions in figure 4 is apparent both in terms of typical magnitudes of fluxes and in terms of their dependence on ε. However, when the analogous comparison was made for $Pr = 0.01$ (not shown), the triad model prediction substantially overestimated the direct numerical fluxes. These observations
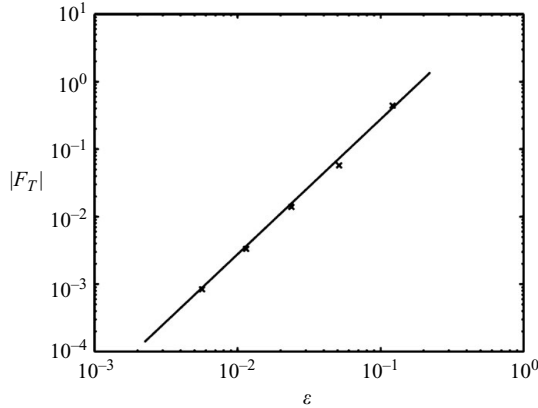
FIGURE 4. The time averaged temperature flux from the direct numerical simulations with $Pr = 1$, $\tau = 1/3$ (x signs) are plotted as a function of $\varepsilon = R_\rho^{-1} - \tau$ in logarithmic coordinates along with the prediction of the asymptotic theory (solid line) based on the triad interaction mechanism.

imply that the triad interaction model performs adequately for moderate and large Pr but fails when Pr is low.

It should also be emphasized that Pr does not even appear in the asymptotic equations (8) and (11), which, at first, may seem to suggest that the Prandtl number effects are secondary. However, such interpretation would be erroneous. Simulations offer plenty of evidence to the contrary – the flow patterns in low Pr regime differ dramatically from those observed for large Pr (see figures 1 and 2). Yet another reason to doubt the relevance of the triad interaction model for low Pr comes from taking the horizontal average of (11). The averaging eliminates all terms on the left-hand side and, making use of the assumed periodic boundary conditions on ψ, we arrive at

$$\bar{\psi}_0(z) = 0, \qquad (14)$$

where bar denotes the horizontal average. Thus, the triad model ignores effects of the mean vertical shear – the most dramatic feature of salt fingering (see figure 2b) and, most likely, a key player in the equilibrium dynamics at low Pr. In order to gain insight into the effects of shear, we now turn to the asymptotic model that is focused specifically on the mean field interaction.

3.2. *Mean field theory*

Mean field models typically assume a two-stage equilibration process: first, nonlinear interaction of the growing unstable modes leads to the modification of the horizontally averaged fields $(\bar{T}, \bar{S}, \bar{\psi})$ and then the mean field modes interact with primary instabilities and suppress their growth. Pursuing this idea, we assume that the principal consequence of the interaction between the leading order modes (5) is the generation of x-independent components. Scales of these components are deduced from the balance between the linear mean field terms in the governing equations (1) and the leading order nonlinearity:

$$\begin{cases} T = \varepsilon^q T_0 + \varepsilon^{2q+\frac{1}{4}}\theta(z) + \dots, \\ S = \varepsilon^q S_0 + \varepsilon^{2q+\frac{1}{4}}\sigma(z) + \dots, \\ \psi = \varepsilon^{q+\frac{1}{4}}\psi_0 + \varepsilon^{2q+\frac{1}{2}}\varphi(z) + \dots. \end{cases} \qquad (15)$$

where $(\theta, \sigma, \varphi)$ are the rescaled mean field variables. Since the first term in the temperature equation $(\partial T/\partial t \sim \varepsilon^{3/2}\varepsilon^q)$ is supposed to be of the same order as the nonlinear advection of the primary instability modes $(\varepsilon^q T_0)$ by the mean shear $(\varepsilon^{2q+1/2}\varphi)$, we arrive at

$$q = \frac{1}{4}. \tag{16}$$

Note that this value is different from q realized in the triad model (6). When series (15) is further extended, we arrive at

$$\begin{cases} T = \varepsilon^{1/4} T_0 + \varepsilon^{3/4}\theta(z) + \varepsilon^{5/4} T_2 + \dots, \\ S = \varepsilon^{1/4} S_0 + \varepsilon^{3/4}\sigma(z) + \varepsilon^{5/4} S_2 + \dots, \\ \psi = \varepsilon^{1/2}\psi_0 + \varepsilon\varphi(z) + \varepsilon^{3/2}\psi_2 + \dots. \end{cases} \tag{17}$$

Next, these series are substituted in governing equations (1) and terms of the same order in ε are collected. The leading order $(\sim\varepsilon^{3/4})$ balance of the advection–diffusion equations yields the diagnostic relationships:

$$\begin{cases} T_0 = S_0, \\ \dfrac{\partial\psi_0}{\partial x_0} = \nabla_0^2 T_0, \end{cases} \tag{18}$$

which are identical to that in the triad model. The first-order $(\sim\varepsilon^{5/4})$ balance of the advection–diffusion equations makes it possible to express the mean T-S components in terms of the zero-order quantities:

$$\begin{cases} \overline{J_0(\psi_0, T_0)} = \dfrac{\partial^2\theta}{\partial_0^2 z_0}, \\ \overline{J_0(\psi_0, T_0)} = \tau\dfrac{\partial^2\sigma}{\partial_0^2 z_0}, \end{cases} \tag{19}$$

whereas at the second order $(\sim\varepsilon^{7/4})$ we obtain

$$\begin{cases} \dfrac{\partial T_0}{\partial t_0} + J_0(\varphi, T_0) + J_0(\psi_0, \theta) + \dfrac{\partial\psi_2}{\partial x_0} = \nabla_0^2 T_2, \\ \dfrac{\partial S_0}{\partial t_0} + J_0(\varphi, S_0) + J_0(\psi_0, \sigma) + \dfrac{\partial\psi_0}{\partial x_0} + \tau\dfrac{\partial\psi_2}{\partial x_0} = \tau\nabla_0^2 S_2. \end{cases} \tag{20}$$

The vorticity equation at the leading $(\sim\varepsilon^{3/2})$ order reduces to

$$\frac{\partial}{\partial x_0}(T_2 - S_2) + \nabla_0^4\psi_0 = 0, \tag{21}$$

and the horizontally averaged second-order $(\sim\varepsilon^2)$ balance of the vorticity equation yields

$$\overline{J_0(\psi_0, \nabla_0^2\psi_0)} = Pr\frac{\partial^4\varphi}{\partial z_0^4}. \tag{22}$$

Our final step is to eliminate the second order terms (T_2, S_2) and form a closed system of equations for zero-order quantities, which is accomplished as follows. The salinity equation in (20) is divided by τ, subtracted from the temperature equation, and then $(T_2 - S_2)$ in the resulting expression is eliminated using (21):

$$\left(\frac{1}{\tau} - 1\right)\frac{\partial}{\partial x_0}\left[\frac{\partial T_0}{\partial t_0} - \frac{\partial\varphi}{\partial z_0}\frac{\partial T_0}{\partial x_0}\right] + \left(\frac{1}{\tau^2} - 1\right)\frac{\partial}{\partial x_0}\left(\frac{\partial\psi_0}{\partial x_0}\frac{\partial\theta}{\partial z_0}\right) + \frac{1}{\tau}\frac{\partial^2\psi_0}{\partial x_0^2} = \nabla_0^6\psi_0. \tag{23}$$

T_0

(a)

z_0

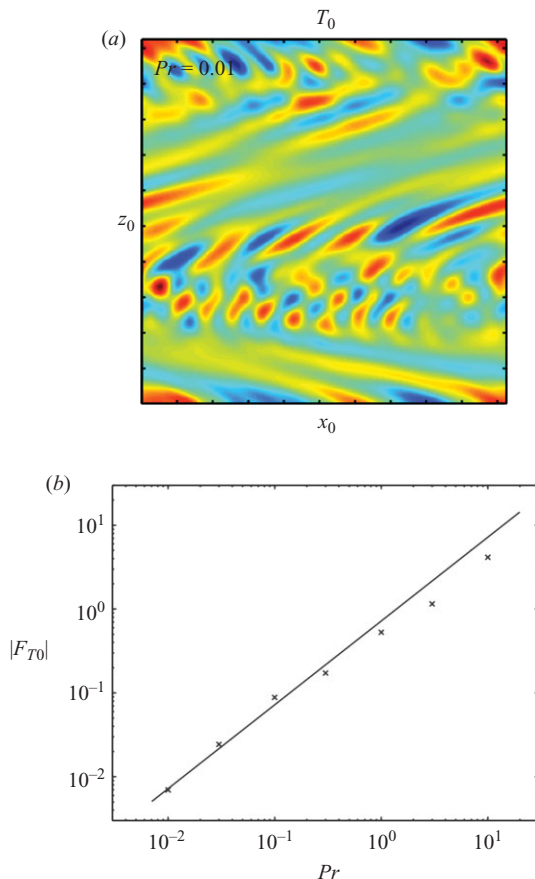$Pr = 0.01$

x_0

(b)

$|F_{T0}|$

Pr

FIGURE 5. Numerical integration of the mean field equations. (*a*) Typical instantaneous temperature field for $Pr = 0.01$, $\tau = 1/3$. (*b*) The rescaled (time averaged) temperature flux from a series of simulations (x signs) with various values of Prandtl number, plotted as a function of Pr in logarithmic coordinates along with the asymptotic ($Pr \rightarrow 0$) prediction (solid line).

The combination of (18), (19), (22) and (23) represents a closed system of equations. To determine whether it captures gross features of the original system (1) at low Prandtl number, the asymptotic model was numerically integrated in time. Figure 5(*a*) present a typical instantaneous temperature field for $Pr = 0.01$ (for consistency, all other parameters were kept the same as in all preceding runs). The temperature patterns simulated by the mean field model have many characteristics in common with the original low-Pr-number calculations (figure 2). In both models, salt fingers appear in the form of disorganized, roughly isotropic blobs, distorted by the background shear flow. However, for large Pr the mean field model solutions (not shown), bear little resemblance to the patterns observed in the corresponding simulations of the original system (figure 1).

Thus, intriguing questions arise: Why is the mean field model more relevant at low Pr but the triad model more appropriate for moderate and large Pr? What determines the point of transition between these two distinct dynamical regimes? Is it possible to incorporate both effects in terms of a unified asymptotic model? To answer the first question, we examine the equilibrium amplitudes predicted by the

mean field and triad models. The two models are characterized by different ε-scales of primary variables, as given in (7) and (17). For instance, the magnitudes of the temperature flux $F_T = \langle wT \rangle$ – a principal measure of the salt finger intensity – are represented by the following leading order scales:

$$\begin{cases} F_{Ttriad} = \varepsilon^2 F_{T0triad}, \\ F_{Tmean-field} = \varepsilon F_{T0mean-field}. \end{cases} \tag{24}$$

These dependencies suggest that if ε is small and $F_{T0triad}$ and $F_{T0mean-field}$ are order one quantities, then $|F_{Ttriad}| \ll |F_{Tmean-field}|$. This, in turn, implies that the equilibration should occur through the triad mechanism: As weak initially linear unstable fingers gradually increase their amplitude, they first reach the magnitude required for the triad equilibration and stop growing, whereas engaging the mean field mechanisms would require further increase in amplitude.

The foregoing argument, however, should be modified for small Pr. Recall that the zero-order quantities in the triad model are independent of Pr, which is not the case for the mean field model. The dependence of the mean field model flux on Pr is shown in figure 5(*b*), which illustrates a strong, nearly linear, relationship between $F_{T0mean-field}$ and Pr. This dependence can be rationalized (see Appendix B) by considering the limit $Pr \to 0$, which at the leading order yields:

$$F_{T0mean-field} = Pr\,F_{T00} \quad \text{for } Pr \to 0, \tag{25}$$

where F_{T00} is independent of Pr. Thus, the equilibrium amplitude for the triad interaction model can actually exceed the mean field equilibrium level if:

$$|F_{Ttriad}| \sim \varepsilon^2 > \varepsilon Pr \sim |F_{Tmean-field}| \quad \to \quad Pr < \varepsilon, \tag{26}$$

resulting in a different equilibrium dynamics – dynamics controlled by the mean horizontal shear. This conjecture rationalizes features observed in the direct numerical simulations and specifies the regions in the parameter space controlled by the triad and mean field effects.

Of course, it is desirable to formulate a unified model that includes both effects in a single framework. For that, we note that the equilibrium values in (24) formally appear at the same order in our expansion as long as $Pr \sim \varepsilon$. Thus, a consistent asymptotic model can be developed by rescaling the Prandtl number as follows:

$$Pr = \varepsilon Pr_0, \tag{27}$$

and the asymptotic solutions in this sector of the parameter space will be presented next.

4. Combined effects of the triad interaction and the mean field

Aside from a different scaling of the Prandtl number, the following theory is analogous to the weakly nonlinear models in §3 and therefore it is presented in abbreviated form.

4.1. *The hybrid weakly nonlinear theory*

The governing equations for the parameter sector (27) consist of the original advection–diffusion equations and the vorticity equation in a slightly modified form:

$$\frac{\partial}{\partial t}\nabla^2\psi + J(\psi, \nabla^2\psi) = Pr_0\varepsilon\left[\frac{\partial}{\partial x}(T - S) + \nabla^4\psi\right]. \tag{28}$$

The independent variables are still rescaled using (4) and the balanced weakly nonlinear solution of this system can be found in terms of an asymptotic expansion (7). The zero-order ($\sim \varepsilon^{5/4}$) and the first-order ($\sim \varepsilon^{9/4}$) balances of T-S equations are identical to those realized in the triad interaction model (see (8) and (9)). However the leading order ($\sim \varepsilon^3$) balance of the vorticity equation (28) is substantially different:

$$\frac{\partial}{\partial t_0} \nabla_0^2 \psi_0 + J_0\left(\psi_0, \nabla_0^2 \psi_0\right) = Pr_0 \left[\frac{\partial}{\partial x_0}(T_1 - S_1) + \nabla^4 \psi_0 \right]. \tag{29}$$

Combining (8), (9) and (29) to eliminate all first-order terms (T_1, S_1, ψ_1), we arrive at

$$\frac{1}{Pr_0} \nabla_0^2 \left[\frac{\partial}{\partial t_0} \nabla_0^2 \psi_0 + J_0\left(\psi_0, \nabla_0^2 \psi_0\right) \right] + \left(\frac{1}{\tau} - 1 \right) \frac{\partial}{\partial x_0} \left[\frac{\partial T_0}{\partial t_0} + J_0(\psi_0, T_0) \right] + \frac{1}{\tau} \frac{\partial^2 \psi_0}{\partial x_0^2} = \nabla_0^6 \psi_0. \tag{30}$$

For convenience, we express the prognostic components in (30) entirely in terms of temperature. For that, we differentiate (30) in x_0 and use the second equation in (8), namely

$$\frac{\partial \psi_0}{\partial x_0} = \nabla_0^2 T_0. \tag{31}$$

It should be emphasized that (31) does not provide a unique solution for ψ_0 in terms of T_0 – what is missing is a prescription for the horizontal average of streamfunction $\overline{\psi_0}$. (This difficulty did not arise in the triad model because of condition (14).) The equation for $\overline{\psi_0}$ is obtained by averaging (29) horizontally. Our final result is a closed system of equations for the zero-order variables:

$$\begin{cases} \dfrac{\partial}{\partial t_0} \left[\left(\dfrac{1}{\tau} - 1 \right) \dfrac{\partial^2 T_0}{\partial x_0^2} + \dfrac{1}{Pr_0} \nabla_0^6 T_0 \right] + \dfrac{1}{Pr_0} \dfrac{\partial}{\partial x_0} \nabla_0^2 J_0\left(\psi_0, \nabla_0^2 \psi_0\right) \\[2mm] \quad + \left(\dfrac{1}{\tau} - 1 \right) \dfrac{\partial^2}{\partial x_0^2} J_0(\psi_0, T_0) + \dfrac{1}{\tau} \dfrac{\partial^2}{\partial x_0^2} \nabla_0^2 T_0 = \nabla_0^8 T_0, \\[2mm] \dfrac{\partial \psi_0}{\partial x_0} = \nabla_0^2 T_0, \\[2mm] \dfrac{\partial}{\partial t_0} \dfrac{\partial^2 \overline{\psi_0}}{\partial z_0^2} + \overline{J_0\left(\psi_0, \nabla_0^2 \psi_0\right)} = Pr_0 \dfrac{\partial^4 \overline{\psi_0}}{\partial z_0^4}. \end{cases} \tag{32}$$

To determine whether this asymptotic limit captures the key properties of the original system (1), the hybrid model was integrated in time. Of particular interest is to observe the transition from the triad equilibration at large Pr to the mean flow dynamics at low Pr. Therefore in the following experiments we varied Pr_0, while other parameters matched earlier simulations. Figure 6(a) presents the typical equilibrium streamfunction pattern for $Pr_0 = 30$. As in large Prandtl number solutions of the original system (figure 1), salt fingers appear in the form of disorganized small-scale filaments, exhibiting no visible signs of the mean shear flow. This homogeneous pattern changes dramatically when Pr_0 is reduced to 0.3 in figure 6(b). The flow field reorganizes into horizontally uniform bands representing the sheared horizontal current, bearing the striking similarity with the corresponding low Prandtl number regime of the original system (figure 2).

Note that the hybrid model (32) was formally derived only for the sector (27) in the (ε, Pr) parameter space where $Pr_0 = O(1)$ and therefore its applicability for a wider
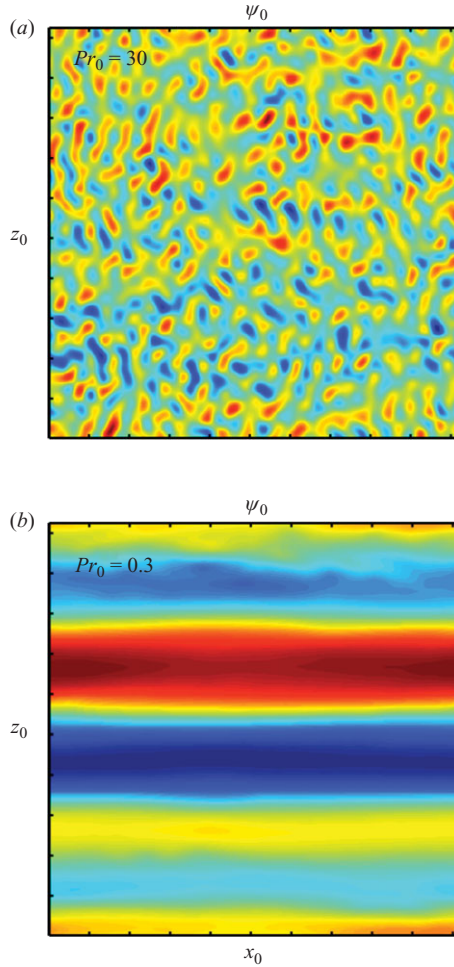
FIGURE 6. The streamfunction field in the hybrid model for (a) $Pr_0 = 30$ and (b) $Pr_0 = 0.3$.

range of Prandtl numbers is yet to be determined. The hybrid model will be validated next by comparing its predictions with the direct numerical simulations of primitive equations (1). However, it should be mentioned that in the limit $Pr_0 \to \infty$ the hybrid model (32) immediately reduces to the triad interaction model. Thus, we expect (32) to be appropriate even for large Prandtl numbers. However for super low values of Prandtl number ($Pr_0 \ll 1$), we anticipate appearance of new effects, not included in the asymptotic formulations, namely the broadband spectrum of modes caused by the separation of the forcing and dissipative scales (see the discussion in Appendix A).

4.2. Comparison with the direct numerical simulations

To systematically discuss utility and limitations of various theoretical models, we now draw together all our asymptotic results and compare them with the corresponding simulations of the original fully nonlinear system (1). Since the asymptotic formulations are based on the expansion in which ε is small, we performed a series of direct numerical simulations with $R_\rho = 2.95$ ($\varepsilon = 0.0056$) and $R_\rho = 2.9$ ($\varepsilon = 0.0115$) and the Prandtl number was systematically varied within the range
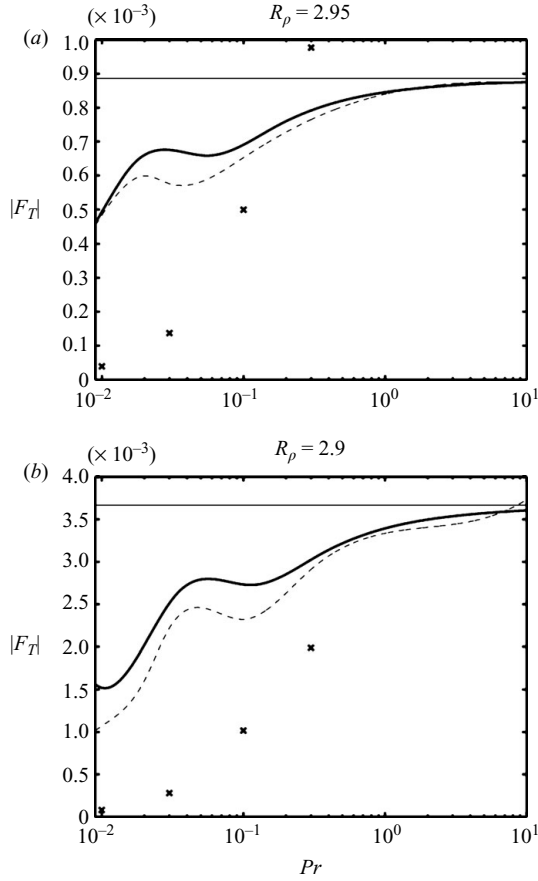
$$0.01 < Pr < 10. \tag{33}$$

FIGURE 7. Comparison of the asymptotic solutions with the direct numerical simulations over a range of Pr for (a) $R_\rho = 2.95$ and (b) $R_\rho = 2.9$. The dashed curves represent the time averaged temperature flux simulated using the original system (1). The corresponding asymptotic fluxes, predicted by the triad, mean field and hybrid models, are indicated by the straight horizontal lines, x signs and heavy curves, respectively.

All other parameters remained the same as in previous simulations (e.g. figures 1 and 2).

The following comparison of models is based on their ability to represent the vertical temperature flux. The fluxes predicted by the triad and mean field models are given by (24), where the rescaled triad flux ($F_{T0triad}$) is in (12) and the rescaled mean field flux ($F_{T0mean-field}$) was computed for Prandtl numbers in the range (33) using (B 1). Prediction of the temperature flux by the hybrid model also required a series of simulations – this time using (32) – in which $Pr_0 = Pr/\varepsilon$ was systematically varied in the range corresponding to (33).

All models, numerical and asymptotic, are compared in figure 7(a) for $R_\rho = 2.95$ and in figure 7(b) for $R_\rho = 2.9$. In each case, the best performance is achieved by the hybrid model (heavy solid curves) which follows closely the pattern of the fully nonlinear simulation (dashed curves) over the entire range of Pr in (33) – the range that spans three orders of magnitude. The numerical simulations and the hybrid model are both characterized by a complicated non-monotonic dependence of the temperature flux on Prandtl number. This agreement indicates that the hybrid model

accurately describes the nonlinear equilibration of salt fingers. Of particular interest is the ability of the hybrid model to capture the transition between two dynamically distinct regimes controlled by the triad and mean field mechanisms. The pure triad model (straight thin lines in figure 7) offers a decent estimate of temperature flux for large values of Pr but fails to capture the variation in fluxes with Prantdl number. The mean field model is least satisfying – it significantly underestimates fluxes for low Pr but overestimates them for large Pr. This suggests that the mean field mechanisms, while undoubtedly essential at low Pr, should always be considered in conjunction with the triad interaction effects.

5. Discussion

This paper presents numerical and theoretical models for the equilibration of weakly nonlinear salt fingers. Two dominant mechanisms of equilibration are the triad interactions between various growing modes and the adverse action of vertical shear, spontaneously developing as a result of secondary salt finger instabilities. Both processes are essential: Triad interactions control the equilibration at moderate and high values of Prandtl number (Pr), whereas the mean field effects become critical at low Pr. The flow characteristics revealed by the direct numerical simulations are explained using an asymptotic expansion in which $\varepsilon = R_\rho^{-1} - \tau$ is small. To gain insight into the mechanics of nonlinear equilibration, we first consider analytical models which isolate the mean field and triad mechanisms (§3). It is shown that, individually, these models cannot accurately describe the equilibrium patterns of salt fingers in all regions of the parameter space. For instance, the triad model captures the essence of the dynamics at play in the sector $Pr \gg \varepsilon$ of governing parameters, which makes it relevant for oceanographic applications ($Pr \sim 10$), but leaves open the possibility of different dynamics in astrophysical systems ($Pr \ll 1$).

To explain the interaction and combined effects of the mean field and triad mechanisms, we propose a hybrid model (§4) which represents both stabilizing processes in a single framework. While this model was originally developed by focusing on a sector in the parameter space for which $Pr \sim \varepsilon$, the resulting solutions agree with the fully nonlinear numerical simulations over a wide range of Pr. Since the hybrid model is about as simple as the triad or mean field models and yet provides a consistent description of both stabilizing mechanisms, it seems sensible to use it under all circumstances as a canonical form for the weakly nonlinear salt fingering. We also note that while specific solutions in this paper are two-dimensional, it is straightforward to extend our asymptotic formulations to three dimensions. The three-dimensional counterparts of the triad, mean field, and hybrid models are presented in Appendix C. It remains to be determined how well these theoretical predictions are realized in three-dimensional direct numerical simulations.

Finally, it should be emphasized that although the weakly nonlinear models in this paper lead to a set of partial differential equations that require further treatment, numerical or analytical, they advance our understanding of double-diffusion in several critical aspects. The central goal of the double-diffusive theory is the prediction of the flow patterns and the vertical transport as a function of three non-dimensional parameters — τ, Pr and R_ρ. The proposed models describe dependence of the system on $\varepsilon = R_\rho^{-1} - \tau$ analytically, thereby reducing the parameter space to just two independent parameters (Pr_0, τ) in case of the hybrid model, or to one (τ) for the triad model. In addition, these nonlinear models offer a transparent interpretation of the processes at play. Complexities of the original (Bousinesq) governing equations

preclude the direct association of individual terms with distinct mechanisms. In contrast, each term in the asymptotic models represents an easily identifiable physics, making it possible to trace the chain of events leading to the nonlinear equilibration of salt fingers. The price paid for tractability is, of course, the limited accuracy outside of the weakly unstable range. In our opinion, it is a fair price.

Appendix A. Linear stability analysis in the limit $\varepsilon \to 0$

Trivial modifications aside, the linear stability analysis yields the same results in three dimensions as it does in two. For simplicity, we use a two-dimensional formulation, in which case the linearization of governing equations (1) yields:

$$
\begin{cases}
\dfrac{\partial T}{\partial t} + \dfrac{\partial \psi}{\partial x} = \nabla^2 T, \\[2mm]
\dfrac{\partial S}{\partial t} + (\varepsilon + \tau)\dfrac{\partial \psi}{\partial x} = \tau \nabla^2 S, \\[2mm]
\dfrac{\partial}{\partial t}\nabla^2 \psi = Pr\left[\dfrac{\partial}{\partial x}(T - S) + \nabla^4 \psi\right],
\end{cases}
\tag{A 1}
$$

where $\varepsilon = 1/R_\rho - \tau$. We now examine the stability characteristics of this system in the limit $\varepsilon \to 0$. Substitution of the normal modes $(\psi, T, S) = (\hat{\psi}, \hat{T}, \hat{S}) \cdot \exp[\mathrm{i}(kx + mz) + \lambda t]$ in (A 1) yields the growth rate equation

$$
\lambda^3 + A\lambda^2 + B\lambda + C = 0,
\tag{A 2}
$$

where

$$
\begin{cases}
A = (k^2 + m^2)(1 + \tau + Pr), \\[2mm]
B = \dfrac{Pr k^2(1 - \tau - \varepsilon)}{k^2 + m^2} + (\tau + \tau Pr + Pr)(k^2 + m^2)^2, \\[2mm]
C = Pr\left[\tau(k^2 + m^2)^3 - \varepsilon k^2\right].
\end{cases}
\tag{A 3}
$$

The cubic equation (A 2) has three roots. Two of the solutions are complex and represent oscillatory modes – gravity waves damped by the molecular dissipation. The third root is real. It represents the direct salt finger instability and therefore, we shall focus on this solution by insisting that the imaginary part of the growth rate is zero: $\mathrm{Im}(\lambda) = 0$. Of particular concern is the maximum growth rate, which is computed by requiring

$$
\left.\frac{\partial}{\partial k}\lambda(k, m)\right|_{\substack{k=k_{max} \\ m=m_{max}}} = \left.\frac{\partial}{\partial m}\lambda(k, m)\right|_{\substack{k=k_{max} \\ m=m_{max}}} = 0.
\tag{A 4}
$$

Differentiating (A 2) in m, we discover that $\partial/\partial m\ \lambda(k, m) = 0$ for $m = 0$, regardless of k. This implies that vertical salt fingers achieve the maximum growth rate and therefore our subsequent analysis is focused on this simple case ($m = 0$), which reduces the growth rate equation (A 2) to

$$
\lambda^3 + k^2(1 + \tau + Pr)\lambda^2 + (\tau Pr k^4 + \tau k^4 + Pr k^4 + Pr - \varepsilon Pr - \tau Pr)\lambda + Pr k^2(\tau k^4 - \varepsilon) = 0.
\tag{A 5}
$$

To determine the horizontal wavenumber of the fastest growing mode (k_{max}), we differentiate (A 5) in k and require the derivative of the growth rate to vanish at $k = k_{max}$:

$$\lambda^2(1 + \tau + Pr) + 2\lambda k_{max}^2(\tau + Pr + \tau Pr) + Pr\left(3\tau k_{max}^4 - \varepsilon\right) = 0. \qquad (A\,6)$$

The fastest growth rate is given by the larger root of the quadratic equation (A6), and its substitution in (A5) yields the equation for k_{max}:

$$a k_{max}^{12} + b k_{max}^8 + c k_{max}^4 + d = 0, \qquad (A\,7)$$

where a, b, c, and d are polynomials (not shown) in τ, Pr, and ε.

Next, we analyse the asymptotic ($\varepsilon \ll 1$) properties of (A 7). Explicit solutions for k_{max} are obtained by expanding in powers of ε as follows:

$$k_{max}^4 = \varepsilon K_1 + \varepsilon^2 K_2 + \dots. \qquad (A\,8)$$

The diffusivity ratio τ in this expansion is regarded as order one quantity. For Prandtl number, it is instructive to consider two limits: (a) $Pr = O(1)$ and (b) $Pr = \varepsilon Pr_0$, where $Pr_0 = O(1)$.

A.1. *Finite Prandtl number*

In this case, substituting series (A 8) in (A 7) and collecting the first-order terms yields

$$K_1 = \frac{1}{3\tau}. \qquad (A\,9)$$

Thus, at the leading order in ε,

$$k_{max} \approx \frac{\varepsilon^{1/4}}{(3\tau)^{1/4}}, \qquad (A\,10)$$

and the corresponding growth rate is evaluated from (A 6):

$$\lambda_{max} \approx \frac{2}{9(1 - \tau)}\sqrt{\frac{3}{\tau}}\varepsilon^{3/2}. \qquad (A\,11)$$

These asymptotic dependencies rationalize the choice of the ε-scales for independent variables (4) used in the weakly nonlinear theory.

A.2. *Low-Prandtl-number limit*

The asymptotic limit considered in the hybrid model (§ 5) involves rescaling the Prandtl number as $Pr = \varepsilon Pr_0$. In this case, substitution of (A 8) in (A 7) and collecting the leading order terms in the resulting expression yields:

$$K_1 = \frac{1}{2\tau}\left(3\tau Pr_0 - 3Pr_0 - 1 + \sqrt{9\tau^2 Pr_0^2 - 18\tau Pr_0^2 - 10\tau Pr_0 + 9Pr_0^2 + 10Pr_0 + 1}\right), \qquad (A\,12)$$

which implies the same asymptotic scalings as in case (a), namely $k_{max} \propto \varepsilon^{1/4}$ and $\lambda_{max} \propto \varepsilon^{3/2}$. Note also that in the limit of large Pr_0, (A 12) converges to (A 9).

It is of interest to also examine the limit of small Pr_0. In this case,

$$K_1 = \frac{1 - \tau}{\tau}Pr_0 + O\left(Pr_0^2\right) \quad \text{for } Pr_0 \to 0, \qquad (A\,13)$$

and the corresponding wavenumber and growth rate reduce to

$$k_{max} \approx \left(\frac{1 - \tau}{\tau}Pr_0\right)^{1/4}\varepsilon^{1/4}, \quad \lambda_{max} \approx \frac{1}{2}\sqrt{\frac{Pr_0}{\tau(1 - \tau)}}(1 - 3Pr_0 + 3\tau Pr_0)\varepsilon^{3/2}. \qquad (A\,14)$$

Thus, k_{max} monotonically decreases with Pr_0 to zero. This property is in contrast with the dependencies of the mode with zero growth rate (k_0), whose wavenumber does not depend on Pr. The latter can be computed from (A 5):

$$k_0 = \frac{\varepsilon^{1/4}}{\tau^{1/4}}. \tag{A 15}$$

The difference in dependencies of k_{max} and k_0 on Pr has potentially significant implications for the nonlinear asymptotic theory in §4. In essence, k_{max} represents the wavelength where the energy and *T-S* variances enter inter the system – the scale of primary salt finger instability. The dissipation range, where molecular processes suppress the growth, starts at k_0. Thus, for $Pr_0 \ll 1$, the forcing scales are separated from the dissipation scales: $k_{max}/k_0 \propto Pr_0^{1/4} \ll 1$. Note that this peculiarity does not arise for moderate and large Pr_0, where necessarily $k_{max}/k_0 = O(1)$.

Hence, we speculate that the process of salt finger equilibration in the limit $Pr_0 \to 0$ involves a cascade of tracer variance to smaller and smaller scales, as occurs in more conventional and fully nonlinear turbulence problems. Consequently, one might anticipate substantial differences between the two-dimensional and three-dimensional solutions. Finally, we add that in the case of super low Prandtl number ($Pr_0 \to 0$), our weakly nonlinear expansion, in its original form, becomes suspect since it assumes a narrow range of spatial scales given by (4). Because of all these hurdles, we do not dare to venture further into the $Pr_0 \ll 1$ regime and limit our asymptotic analysis to moderate and large values of Pr_0.

Appendix B. Weakly nonlinear mean field model in the limit of low Prandtl number

Governing equations for the mean field model discussed in §3.2 are given by

$$\begin{cases} \left(\dfrac{1}{\tau} - 1\right)\dfrac{\partial}{\partial x_0}\left[\dfrac{\partial T_0}{\partial t_0} - \dfrac{\partial \varphi}{\partial z_0}\dfrac{\partial T_0}{\partial x_0}\right] + \left(\dfrac{1}{\tau^2} - 1\right)\dfrac{\partial}{\partial x_0}\left(\dfrac{\partial \psi_0}{\partial x_0}\dfrac{\partial \theta}{\partial z_0}\right) + \dfrac{1}{\tau}\dfrac{\partial^2 \psi_0}{\partial x_0^2} = \nabla_0^6 \psi_0, \\[3mm] \overline{J_0(\psi_0, \nabla_0^2\psi_0)} = Pr\,\dfrac{\partial^4 \varphi}{\partial z_0^4}, \\[3mm] \dfrac{\partial \psi_0}{\partial x_0} = \nabla_0^2 T_0, \\[3mm] \overline{J_0(\psi_0, T_0)} = \dfrac{\partial^2 \theta}{\partial_0^2 z_0} = \tau\,\dfrac{\partial^2 \sigma}{\partial_0^2 z_0}, \end{cases} \tag{B 1}$$

and we are concerned by its behaviour in the limit $Pr \to 0$. If the dominant stabilizing effect in this system is associated with the distortion of salt fingers by the mean shear, then the term $(\partial\varphi/\partial z_0)(\partial T_0/\partial x_0)$ should be of the same order as $\partial T_0/\partial t_0$, which requires φ to be an order one quantity regardless of Pr. The second equation in (B 1) then demands $\psi_0 \sim Pr^{1/2}$; third equation implies that $T_0 \sim Pr^{1/2}$, and fourth – that $(\theta, \sigma) \sim Pr$. Therefore, we rescale variables as follows:

$$\begin{cases} \psi_0 = Pr^{1/2}\psi_{00}, \\ T_0 = Pr^{1/2}T_{00}, \\ \varphi = \varphi_{00}, \\ (\theta, \sigma) = Pr(\theta_{00}, \sigma_{00}), \end{cases} \tag{B 2}$$

where the subscript '00' is used to denote the order one quantities for the limit $Pr \to 0$.

Substituting (B 2) in (B 1) and taking the limit $Pr \rightarrow 0$, we arrive at a new closed system:

$$\begin{cases} \left(\dfrac{1}{\tau} - 1\right) \dfrac{\partial}{\partial x_0} \left[\dfrac{\partial T_{00}}{\partial t_0} - \dfrac{\partial \varphi_{00}}{\partial z_0} \dfrac{\partial T_{00}}{\partial x_0}\right] + \dfrac{1}{\tau} \dfrac{\partial^2 \psi_{00}}{\partial x_0^2} = \nabla_0^6 \psi_{00}, \\[3mm] \overline{J_0\left(\psi_{00}, \nabla_0^2 \psi_{00}\right)} = \dfrac{\partial^4 \varphi_{00}}{\partial z_0^4}, \\[3mm] \dfrac{\partial \psi_{00}}{\partial x_0} = \nabla_0^2 T_{00}. \end{cases} \qquad (B\,3)$$

To determine whether this model is consistent with finite Pr system, (B 3) was numerically integrated in time. For consistency with all other simulations in this paper, the size of the computational domain corresponded to 16×16 fastest growing finger wavelengths, resolved by (128×128) elements, the diffusivity ratio was $\tau = 1/3$, and the model was initialized from rest by a random computer-generated initial T_{00} distribution. After a few characteristic growth periods, active statistically steady double-diffusive convection was established, which exhibits (not shown) all signatures of the finite Pr mean field model – salt fingers appear in the form of disorganized tilted eddies advected by the background shear flow.

To be more quantitative in comparing the asymptotic (B 3) and finite Pr (B 1) simulations, we examine the rescaled temperature flux $F_{T00} = \langle w_{00} T_{00} \rangle$. The time mean value of the equilibrium flux is

$$F_{T00} \approx -0.7217. \qquad (B\,4)$$

The asymptotic ($Pr \rightarrow 0$) prediction for fluxes $F_{T0mean-field} = Pr\, F_{T00}$ is indicated by solid line in figure 5(b), along with the corresponding fluxes from the finite Pr simulations (marked by x signs). The apparent agreement between these calculations supports the foregoing theory and its prescription (25) for the temperature flux in the mean field model.

Appendix C. Three-dimensional formulations

This paper is focused on two-dimensional dynamics – an approach motivated by considerations of computational convenience. In two dimensions, it is possible to efficiently explore the model dependencies over a wide range of governing parameters, whereas three-dimensional simulations of double-diffusion still represent a formidable challenge and are usually performed only for an isolated set, very rarely a few sets, of governing parameters. However, all our theoretical developments can be readily extended to three dimensions. In expectation of utilizing them in future explorations of salt fingering, three-dimensional asymptotics are presented below. Since the derivation of these models closely follows their two-dimensional counterparts, we omit details and present the final results.

The governing – non-dimensional Bousinesq – equations are

$$\begin{cases} \dfrac{\mathrm{d}T}{\mathrm{d}t} + w = \nabla^2 T, \\[3mm] \dfrac{\mathrm{d}S}{\mathrm{d}t} + \dfrac{w}{R_\rho} = \tau \nabla^2 S, \\[3mm] \nabla \cdot \boldsymbol{v} = 0, \\[3mm] \dfrac{\mathrm{d}\boldsymbol{v}}{\mathrm{d}t} = Pr\left[-\nabla p + \dfrac{\partial}{\partial x}(T - S)\boldsymbol{k} + \nabla^2 \boldsymbol{v}\right], \end{cases} \qquad (C\,1)$$

where $\boldsymbol{v} = (u, \mathrm{v}, w)$ is the velocity vector, $p = p_{dim}d^2/\rho_0 \nu k_T$ is the non-dimensional pressure, and $\mathrm{d}/\mathrm{d}t = \partial/\partial t + \boldsymbol{v} \cdot \nabla$ is the material derivative. The space/time scales of independent variables in the limit $\varepsilon = R_\rho^{-1} - \tau \to 0$ are analogous to those in two-dimensions (4):

$$(x, y, z) = \varepsilon^{-1/4}(x_0, y_0, z_0), \quad t = \varepsilon^{-3/2}t_0. \tag{C 2}$$

C.1. *Triad interaction model*
The primary variables are expanded in ε as follows

$$\begin{cases} (T, S) = \varepsilon^{3/4}(T_0, S_0) + \varepsilon^{7/4}(T_1, S_1) + \dots, \\ (u, v, w) = \varepsilon^{5/4}(u_0, v_0, w_0) + \varepsilon^{9/4}(u_1, v_1, w_1) + \dots, \\ p = \varepsilon^{3/2}p_0 + \varepsilon^{5/2}p_1 + \dots, \end{cases} \tag{C 3}$$

and the closed set of asymptotic equations for zero-order variables is given by

$$\begin{cases} \left(\dfrac{1}{\tau} - 1\right)\left[\dfrac{\partial T_0}{\partial t_0} + \nabla_0 \cdot (\boldsymbol{v}_0 T_0)\right] + \dfrac{w_0}{\tau} = -\dfrac{\partial}{\partial z_0}\nabla_0^2 p_0 + \nabla_0^4 w_0, \\ w_0 = \nabla_0^2 T_0, \\ \nabla_h^2 p_0 = -\dfrac{\partial}{\partial z_0}\nabla_0^4 T_0, \quad \dfrac{\partial^3}{\partial z_0^3}\bar{p}_0 = \left(1 - \dfrac{1}{\tau}\right)\dfrac{\partial}{\partial z_0}\overline{w_0 T_0}, \\ \nabla_0^2(u_0, v_0) = \left(\dfrac{\partial p_0}{\partial x_0}, \dfrac{\partial p_0}{\partial y_0}\right), \end{cases} \tag{C 4}$$

where $\nabla_h^2 \equiv (\partial^2/\partial x_0^2) + (\partial^2/\partial y_0^2)$.

C.2. *Mean field model*
The primary variables are expanded in ε as follows:

$$\begin{cases} (T, S) = \varepsilon^{1/4}(T_0, S_0) + \varepsilon^{3/4}(\theta(z), \sigma(z)) + \varepsilon^{5/4}(T_2, S_2) + \dots, \\ (u, v, w) = \varepsilon^{3/4}(u_0, v_0, w_0) + \varepsilon^{5/4}(u_1(z), v_1(z), 0) + \varepsilon^{7/4}(u_2, v_2, w_2) + \dots, \\ p = \varepsilon p_0 + \varepsilon^{3/2}p_1 + \varepsilon^2 p_2 + \dots, \end{cases} \tag{C 5}$$

and the closed set of asymptotic equations for zero-order variables is given by

$$\begin{cases} \left(\dfrac{1}{\tau} - 1\right)\left[\dfrac{\partial T_0}{\partial t_0} + u_1\dfrac{\partial T_0}{\partial x_0} + v_1\dfrac{\partial T_0}{\partial y_0}\right] + \left(\dfrac{1}{\tau^2} - 1\right)w_0\dfrac{\partial \theta}{\partial z_0} + \dfrac{w_0}{\tau} = -\dfrac{\partial}{\partial z_0}\nabla_0^2 p_0 + \nabla_0^4 w_0, \\ w_0 = \nabla_0^2 T_0, \\ \nabla_h^2 p_0 = -\dfrac{\partial}{\partial z_0}\nabla_0^4 T_0, \quad \bar{p}_0 = 0, \\ \nabla_0^2(u_0, v_0) = \left(\dfrac{\partial p_0}{\partial x_0}, \dfrac{\partial p_0}{\partial x_0}\right), \\ \nabla_0^2(u_1, v_1) = \dfrac{1}{Pr}(\overline{w_0 u_0}, \overline{w_0 v_0}). \end{cases} \tag{C 6}$$

C.3. *Hybrid model*

The primary variables are expanded in ε as in (C 3) and the closed set of asymptotic equations for zero-order variables is given by

$$
\begin{cases}
\left(\dfrac{1}{\tau}-1\right)\left[\dfrac{\partial T_0}{\partial t_0}+\nabla_0\cdot(\boldsymbol{v}_0 T_0)\right]+\dfrac{1}{Pr_0}\nabla_0^2\left[\dfrac{\partial \nabla_0^2 T_0}{\partial t_0}+\nabla_0\cdot(\boldsymbol{v}_0\nabla_0^2 T)\right]+\dfrac{w_0}{\tau}, \\
\quad=-\dfrac{\partial}{\partial z_0}\nabla_0^2 p_0+\nabla_0^4 w_0,\ w_0=\nabla_0^2 T_0, \\
\nabla_h^2 p_0=-\dfrac{\partial}{\partial z_0}\nabla_0^4 T_0,\ \dfrac{\partial^3}{\partial z_0^3}\bar{p}_0=\left(1-\dfrac{1}{\tau}\right)\dfrac{\partial}{\partial z_0}\overline{w_0 T_0}+\dfrac{1}{Pr_0}\dfrac{\partial^3}{\partial z_0^3}\overline{w_0\nabla_0^2 T}, \\
\nabla_0^2(u_0,v_0)=\left(\dfrac{\partial p_0}{\partial x_0},\dfrac{\partial p_0}{\partial x_0}\right).
\end{cases}
\tag{C 7}
$$

REFERENCES

BALMFORTH, N. J., GHADGE, S. A., KETTAPUN, A. & MANDRE, S. D. 2006 Bounds on double-diffusive convection. *J. Fluid Mech.* **569**, 29–50.

CHARBONNEL, C. & ZAHN, J. 2007 Thermohaline mixing: a physical mechanism governing the photospheric composition of low-mass giants. *Astron. Astrophys.* **467**, L29–L32.

DRAZIN, P. G. & REID, W. H. 1981 *Hydrodynamic Stability*. Cambridge University Press, p. 527.

GUILLOT, T. 1999 Interiors of giant planets inside and outside the solar system. *Science* **286**, 72–77.

HOLYER, J. Y. 1984 The stability of long steady, two-dimensional salt fingers. *J. Fluid Mech.* **147**, 169–185.

HOWARD, L. N. & KRISHNAMURTI, R. 1986 Large scale flow in turbulent convection: a mathematical model. *J. Fluid Mech.* **170**, 385–419.

KRISHNAMURTI, R. 2003 Double-diffusive transport in laboratory thermohaline staircases. *J. Fluid Mech.* **483**, 287–314.

KRISHNAMURTI, R. & HOWARD, L. N. 1981 Large scale flow in turbulent convection. *Proc. Natl Acad. Sci. USA* **78**, 1981–1985.

LANDAU, L. D. 1944 On the problem of turbulence. *Dokl. Akad. Nauk SSSR.* **44**, 311–314.

MALKUS, W. V. R. & VERONIS, G. 1958 Finite amplitude cellular convection. *J. Fluid Mech.* **4**, 225–260.

MERRYFIELD, W. J. 1995 Hydrodynamics of semiconvection. *Astrophys. J.* **444**, 318–337.

MERRYFIELD, W. J. 2000 Origin of thermohaline staircases. *J. Phys. Oceanogr.* **30**, 1046–1068.

PROCTOR, M. R. E. & HOLYER, J. Y. 1986 Planform selection in salt fingers. *J. Fluid Mech.* **168**, 241–253.

RADKO, T. 2003 A mechanism for layer formation in a double-diffusive fluid. *J. Fluid Mech.* **497**, 365–380.

RADKO, T. 2005 What determines the thickness of layers in a thermohaline staircase? *J. Fluid Mech.* **523**, 79–98.

RADKO, T. 2008 The double-diffusive modon. *J. Fluid Mech.* **609**, 59–85.

RADKO, T. & STERN, M. E. 1999 Salt fingers in three dimensions. *J. Mar. Res.* **57**, 471–502.

RADKO, T. & STERN, M. E. 2000 Finite amplitude salt fingers in a vertically bounded layer. *J. Fluid Mech.* **425**, 133–160.

SCHMITT, R. W. 1979 The growth rate of supercritical salt fingers. *Deep-Sea Res.* **26A**, 23–44.

SCHMITT, R. 1983 The characteristics of salt fingers in a variety of fluid systems, including stellar interiors, liquid metals, oceans, and magmas. *Phys. Fluids* **26**, 2373–2377.

STANCLIFFE, R., GLEBBEEK, E., IZZARD, R. & POLS, O. 2007 Carbon-enhanced metal-poor stars and thermohaline mixing. *Astron. Astrophys.* **464**, L57–L60.

STERN, M. E. 1960 The "salt-fountain" and thermohaline convection. *Tellus* **12**, 172–175.

STERN, M. E. & RADKO, T. 1998 The salt finger amplitude in unbounded T-S gradient layers. *J. Mar. Res.* **56**, 157–196.

STERN, M. E., RADKO, T. & SIMEONOV, J. 2001 Three-dimensional salt fingers in an unbounded thermocline with application to the Central Ocean. *J. Mar. Res.* **59**, 355–390.

STERN, M. E. & SIMEONOV, J. 2005 The secondary instability of salt fingers. *J. Fluid Mech.* **533**, 361–380.

TAIT, S. & JAUPART, C. 1989 Compositional convection in viscous melts. *Nature* **338**, 571–574.

VAUCLAIR, S. 2004 Metallic fingers and metallicity excess in exoplanets' host stars: the accretion hypothesis revisited. *Astrophys. J.* **605**, 874–879.

VERONIS, G. 1965 On finite amplitude instability in thermohaline convection. *J. Mar. Res.* **23**, 1–17.